

Hole spin relaxation and coefficients in Landau-Lifshitz-Gilbert equation in ferromagnetic GaMnAs

K. Shen and M. W. Wu*

*Hefei National Laboratory for Physical Sciences at Microscale and Department of Physics,
University of Science and Technology of China, Hefei, Anhui, 230026, China*

(Dated: February 18, 2022)

We investigate the temperature dependence of the coefficients in the Landau-Lifshitz-Gilbert equation in ferromagnetic GaMnAs by employing the Zener model. We first calculate the hole spin relaxation time based on the microscopic kinetic equation. We find that the hole spin relaxation time is typically several tens femtoseconds and can present a nonmonotonic temperature dependence due to the variation of the interband spin mixing, influenced by the temperature related Zeeman splitting. With the hole spin relaxation time, we are able to calculate the coefficients in the Landau-Lifshitz-Gilbert equation, such as the Gilbert damping, nonadiabatic spin torque, spin stiffness and vertical spin stiffness coefficients. We find that the nonadiabatic spin torque coefficient β is around $0.1 \sim 0.3$ at low temperature, which is consistent with the experiment [Adam *et al.*, Phys. Rev. B **80**, 193204 (2009)]. As the temperature increases, β monotonically increases and can exceed one in the vicinity of the Curie temperature. In the low temperature regime with $\beta < 1$, the Gilbert damping coefficient α increases with temperature, showing good agreement with the experiments [Sinova *et al.*, Phys. Rev. B **69**, 085209 (2004); Khazen *et al.*, *ibid.* **78**, 195210 (2008)]. Furthermore, we predict that α decreases with increasing temperature once $\beta > 1$ near the Curie temperature. We also find that the spin stiffness decreases with increasing temperature, especially near the Curie temperature due to the modification of the finite β . Similar to the Gilbert damping, the vertical spin stiffness coefficient is also found to be nonmonotonically dependent on the temperature.

PACS numbers: 72.25.Rb, 75.50.Pp, 72.25.Dc, 75.30.Gw

I. INTRODUCTION

The ferromagnetic semiconductor, GaMnAs, has been proposed to be a promising candidate to realize all-semiconductor spintronic devices,^{1,2} where the existence of the ferromagnetic phase in the heavily doped sample sustains seamless spin injection and detection in normal non-magnetic semiconductors.^{3,4} One important issue for such applications lies in the efficiency of the manipulation of the macroscopic magnetization, which relies on properties of the magnetization dynamics. Theoretically, the magnetization dynamics can be described by the extended Landau-Lifshitz-Gilbert (LLG) equation,⁵⁻¹⁰

$$\begin{aligned} \dot{\mathbf{n}} = & -\gamma \mathbf{n} \times \mathbf{H}_{\text{eff}} + \alpha \mathbf{n} \times \dot{\mathbf{n}} - (1 - \beta \mathbf{n} \times) (\mathbf{v}_s \cdot \nabla) \mathbf{n} \\ & - \frac{\gamma}{M_d} \mathbf{n} \times (A_{\text{ss}} - A_{\text{ss}}^v \mathbf{n} \times) \nabla^2 \mathbf{n}, \end{aligned} \quad (1)$$

with \mathbf{n} and M_d standing for the direction and magnitude of the magnetization, respectively. \mathbf{H}_{eff} is the effective magnetic field and/or the external field. The second term on the right hand side of the equation is the Gilbert damping torque with α denoting the damping coefficient.^{5,6} The third one describes the spin-transfer torque induced by the spin current \mathbf{v}_s .^{7,8} As reported, the out-of-plane contribution of the spin-transfer torque, measured by the nonadiabatic torque coefficient β , can significantly ease the domain wall motion.^{7,8} In Eq. (1), the spin stiffness and vertical spin stiffness coefficients are evaluated by A_{ss} and A_{ss}^v respectively, which are essentially important for the static structure of the magnetic domain wall.¹⁰ Therefore, for a thorough understanding

of properties of the magnetization dynamics, the exact values of the above coefficients are required.

In the past decade, the Gilbert damping and nonadiabatic torque coefficients have been derived via many microscopic approaches, such as the Blotzmann equation,¹¹ diagrammatic calculation,^{12,13} Fermi-surface breathing model¹⁴⁻¹⁶ and kinetic spin Bloch equations.^{10,17} According to these works, the spin lifetime of the carriers was found to be critical to both α and β . However, to the best of our knowledge, the microscopic calculation of the hole spin lifetime in ferromagnetic GaMnAs is still absent in the literature, which prevents the determination of the values of α and β from the analytical formulas. Alternatively, Sinova *et al.*¹⁸ identified the Gilbert damping from the susceptibility diagram of the linear-response theory and calculated α as function of the quasiparticle lifetime and the hole density. Similar microscopic calculation on β was later given by Garate *et al.*¹⁹ In those works, the quasiparticle lifetime was also treated as a parameter instead of explicit calculation. Actually, the accurate calculation of the hole spin and/or quasiparticle lifetime in ferromagnetic GaMnAs is difficult due to the complex band structure of the valence bands. In the present work, we employ the microscopic kinetic equation to calculate the spin lifetime of the hole gas and then evaluate α and β in ferromagnetic GaMnAs. For the velocity of the domain-wall motion due to the spin current, the ratio β/α is an important parameter, which has attracted much attention.^{12,19,20} Recently, a huge ratio (~ 100) in nanowire was predicted from the calculation of the scattering matrix by Hals *et al.*²⁰ By calculating α and β , we

are able to supply detailed information of this interesting ratio in bulk material. Moreover, the peak-to-peak ferromagnetic resonance measurement revealed pronounced temperature and sample preparation dependences of the Gilbert damping coefficient.^{18,21,22} For example, in annealed samples, α can present an increase in the vicinity of the Curie temperature,^{18,21} which has not been studied theoretically in the literature. Here, we expect to uncover the underlying physics of these features. In addition, the nonadiabatic torque coefficient β in GaMnAs has been experimentally determined from the domain-wall motion and quite different values were reported by different groups, from 0.01 to 0.36,^{23,24} which need to be verified by the microscopic calculation also. Moreover, to the best of our knowledge, the temperature dependence of β has not been studied theoretically. We will also address this issue in the present work.

In the literature, the spin stiffness in GaMnAs was studied by König *et al.*,^{25,26} who found that A_{ss} increases with hole density due to the stronger carrier-mediated interaction between magnetic ions, i.e., $A_{ss} = N_h/(4m^*)$ with N_h and m^* being the density and effective mass of hole gas, separately. However, as shown in our previous work, the stiffness should be modified as $A_{ss} \sim N_h/[4m^*(1+\beta^2)]$ in ferromagnetic GaMnAs with a finite β .¹⁰ As a result, A_{ss} as well as the vertical spin stiffness $A_{ss}^v = \beta A_{ss}$ may show a temperature dependence introduced by β . This is also a goal of the present work.

For a microscopic investigation of the hole dynamics, the valence band structure is required for the description of the occupied carrier states. In the literature, the Zener model²⁷ based on the mean-field theory has been widely used for itinerant holes in GaMnAs,²⁸⁻³¹ where the valence bands split due to the mean-field p - d exchange interaction. In the present work, we utilize this model to calculate the band structure with the effective Mn concentration from the experimental value of the low-temperature saturate magnetization in GaMnAs. The thermal effect on the band structure is introduced via the temperature dependence of the magnetization following the Brillouin function. Then we obtain the hole spin relaxation time by numerically solving the microscopic kinetic equations with the relevant hole-impurity and hole-phonon scatterings. The carrier-carrier scattering is neglected here by considering the strongly degenerate distribution of the hole gas below the Curie temperature. We find that the hole spin relaxation time decreases/increases with increasing temperature in the small/large Zeeman splitting regime, which mainly results from the variation of the interband spin mixing. Then we study the temperature dependence of the coefficients in the LLG equation, i.e., α , β , A_{ss} and A_{ss}^v , by using the analytical formulas derived in our previous works.^{10,17} Specifically, we find that β increases with increasing temperature and can exceed one in the vicinity of the critical point, resulting in very interesting behaviors of other coefficients. For example, α can present an interesting nonmonotonic temperature dependence with

the crossover occurring at $\beta \sim 1$. Specifically, α increases with temperature in the low temperature regime, which is consistent with the experiments. Near the Curie temperature, an opposite temperature dependence of α is predicted. Similar nonmonotonic behavior is also predicted in the temperature dependence of A_{ss}^v . Our results of β and A_{ss} also show good agreement with the experiments.

This work is organized as follows. In Sec. II, we setup our model and lay out the formulism. Then we show the band structure from the Zener model and the hole spin relaxation time from microscopic kinetic equations in Sec. III. The temperature dependence of the Gilbert damping, nonadiabatic spin torque, spin stiffness and vertical spin stiffness coefficients are also shown in this section. Finally, we summarize in Sec. IV.

II. MODEL AND FORMULISM

In the sp - d model, the Hamiltonian of hole gas in GaMnAs is given by³¹

$$H = H_p + H_{pd}, \quad (2)$$

with H_p describing the itinerant holes. H_{pd} is the sp - d exchange coupling. By assuming that the momentum \mathbf{k} is still a good quantum number for itinerant hole states, one employs the Zener model and utilizes the $\mathbf{k} \cdot \mathbf{p}$ perturbation Hamiltonian to describe the valence band states. Specifically, we take the eight-band Kane Hamiltonian $H_K(\mathbf{k})$ (Ref. 32) in the present work. The sp - d exchange interaction reads

$$H_{pd} = -\frac{1}{N_0 V} \sum_l \sum_{mm'\mathbf{k}} J_{\text{ex}}^{mm'} \mathbf{S}_l \cdot \langle m\mathbf{k} | \hat{\mathcal{J}} | m'\mathbf{k} \rangle c_{m\mathbf{k}}^\dagger c_{m'\mathbf{k}}, \quad (3)$$

with N_0 and V standing for the density of cation sites and the volume, respectively. The cation density $N_0 = 2.22 \times 10^{22} \text{ cm}^{-3}$. The eight-band spin operator can be written as $\hat{\mathcal{J}} = (\frac{1}{2}\boldsymbol{\sigma}) \oplus \mathbf{J}_{3/2} \oplus \mathbf{J}_{1/2}$, where $\frac{1}{2}\boldsymbol{\sigma}$, $\mathbf{J}_{3/2}$ and $\mathbf{J}_{1/2}$ represent the total angular momentum operators of the conduction band, Γ_8 valence band and Γ_7 valence band, respectively. $J_{\text{ex}}^{mm'}$ stands for the matrix element of the exchange coupling, with $\{m\}$ and $\{m'\}$ being the basis defined as the eigenstates of the angular momentum operators $\hat{\mathcal{J}}$. The summation of “ l ” is through all localized Mn spins \mathbf{S}_l (at \mathbf{r}_l).

Then we treat the localized Mn spin in a mean-field approximation and obtain

$$\bar{H}_{pd} = -x_{\text{eff}} \langle \mathbf{S} \rangle \cdot \left(\sum_{mm'\mathbf{k}} J_{\text{ex}}^{mm'} \langle m\mathbf{k} | \hat{\mathcal{J}} | m'\mathbf{k} \rangle c_{m\mathbf{k}}^\dagger c_{m'\mathbf{k}} \right), \quad (4)$$

where $\langle \mathbf{S} \rangle$ represents the average spin polarization of Mn atoms with uncompensated doping density $N_{\text{Mn}} = x_{\text{eff}} N_0$. Obviously, \bar{H}_{pd} can be reduced into three blocks as $\hat{\mathcal{J}}$, i.e., $\bar{H}_{pd}^{mm'}(\mathbf{k}) = \Delta^{mm} \mathbf{n} \cdot \langle m\mathbf{k} | \hat{\mathcal{J}} | m'\mathbf{k} \rangle$ with the Zeeman splitting of the m -band $\Delta^{mm} = -x_{\text{eff}} S_d J_{\text{ex}}^{mm} \frac{M(T)}{M(0)}$.

Here, \mathbf{n} is the direction of $\langle \mathbf{S} \rangle$. For a manganese ion, the total spin $S_d = 5/2$. The temperature-dependent spontaneous magnetization $M(T)$ can be obtained from the following equation of the Brillouin function³³

$$B_{S_d}(y) = \frac{S_d + 1}{3S_d} \frac{T}{T_c} y, \quad (5)$$

where $y = \frac{3S_d}{S_d+1} \frac{M(T)}{M(0)} \frac{T}{T_c}$ with T_c being the Curie temperature. Here, $B_{S_d}(y) = \frac{2S_d+1}{2S_d} \coth(\frac{2S_d+1}{2S_d} y) - \frac{1}{2S_d} \coth(\frac{1}{2S_d} y)$.

The Schrödinger equation of the single particle Hamiltonian is then written as

$$[H_K(\mathbf{k}) + \bar{H}_{pd}(\mathbf{k})]|\mu, \mathbf{k}\rangle = E_{\mu\mathbf{k}}|\mu, \mathbf{k}\rangle. \quad (6)$$

One obtains the band structure and wave functions from the diagonalization scheme. In the presence of a finite Zeeman splitting, the structure of the valence bands deviates from the parabolic dispersion and becomes strongly anisotropic as we will show in the next section. Moreover, the valence bands at Fermi surface are well separated in ferromagnetic GaMnAs because of the high hole density ($> 10^{20} \text{ cm}^{-3}$) and Zeeman splitting, suggesting that the Fermi golden rule can be used to calculate the lifetime of the quasiparticle states. For example, the contribution of the hole-impurity scattering on the μ th-band state with energy ϵ can be expressed by

$$[\tau_{\mu,p}^{hi}(\epsilon)]^{-1} = 2\pi \sum_{\nu} \frac{n_i}{D_{\mu}(\epsilon)} \int \frac{d^3k}{(2\pi)^3} \int \frac{d^3q}{(2\pi)^2} \delta(\epsilon - \epsilon_{\mu\mathbf{k}}) \times \delta(\epsilon_{\mu\mathbf{k}} - \epsilon_{\nu\mathbf{q}}) U_{\mathbf{k}-\mathbf{q}}^2 |\langle \mu\mathbf{k} | \nu\mathbf{q} \rangle|^2 f(\epsilon_{\mu\mathbf{k}}) [1 - f(\epsilon_{\nu\mathbf{q}})], \quad (7)$$

where $D_{\mu}(\epsilon)$ stands for the density of states of the μ th band. $f(\epsilon_{\mu\mathbf{k}})$ satisfies the Fermi distribution in the equilibrium state. The hole-impurity scattering matrix element $U_{\mathbf{q}}^2 = Z^2 e^4 / [\kappa_0 (q^2 + \kappa^2)]^2$ with $Z = 1$. κ_0 and κ denote the static dielectric constant and the screening constant under the random-phase approximation,³⁴ respectively. Similar expression can also be obtained for the hole-phonon scattering.

However, it is very complicated to carry out the multi-fold integrals in Eq. (7) numerically for an anisotropic dispersion. Also the lifetime of the quasiparticle is not equivalent to the spin lifetime of the whole system, which is required to calculate the LLG coefficients according to our previous work.^{10,17} Therefore, we extend our kinetic spin Bloch equation approach³⁵ to the current system to study the relaxation of the total spin polarization as follows. By taking into account the finite separation between different bands, one neglects the interband coherence and focuses on the carrier dynamics of the non-equilibrium population. The microscopic kinetic equation is then given by

$$\partial_t n_{\mu,\mathbf{k}} = \partial_t n_{\mu,\mathbf{k}}|^{hi} + \partial_t n_{\mu,\mathbf{k}}|^{hp}, \quad (8)$$

with $n_{\mu,\mathbf{k}}$ being the carrier occupation factor at the μ th band with momentum \mathbf{k} . The first and second terms on

the right hand side stand for the hole-impurity and hole-phonon scatterings, respectively. Their expressions can be written as

$$\begin{aligned} \partial_t n_{\mu,\mathbf{k}}|^{hi} &= -2\pi n_i \sum_{\nu,\mathbf{k}'} U_{\mathbf{k}-\mathbf{k}'}^2 (n_{\mu\mathbf{k}} - n_{\nu\mathbf{k}'}) |\langle \mu\mathbf{k} | \nu\mathbf{k}' \rangle|^2 \\ &\times \delta(E_{\mu\mathbf{k}} - E_{\nu\mathbf{k}'}), \end{aligned} \quad (9)$$

and

$$\begin{aligned} \partial_t n_{\mu,\mathbf{k}}|^{hp} &= -2\pi \sum_{\lambda,\pm,\nu,\mathbf{k}'} |M_{\mathbf{k}-\mathbf{k}'}^{\lambda}|^2 \delta(E_{\nu\mathbf{k}'} - E_{\mu\mathbf{k}} \pm \omega_{\lambda,\mathbf{q}}) \\ &\times [N_{\lambda,\mathbf{q}}^{\pm} (1 - n_{\nu\mathbf{k}'}) n_{\mu\mathbf{k}} - N_{\lambda,\mathbf{q}}^{\mp} n_{\nu\mathbf{k}'} (1 - n_{\mu\mathbf{k}})] |\langle \mu\mathbf{k} | \nu\mathbf{k}' \rangle|^2 \end{aligned} \quad (10)$$

with $N_{\lambda,\mathbf{q}}^{\pm} = [\exp(\omega_{\lambda,\mathbf{q}}/k_B T) - 1]^{-1} \pm \frac{1}{2}$. The details of the hole-phonon scattering elements $|M_{\mathbf{q}}^{\lambda}|^2$ can be found in Refs. 36–38. From an initial condition with a small non-equilibrium distribution, the temporal evolution of the hole spin polarization is carried out by

$$\mathcal{J}(t) = \frac{1}{N_h} \sum_{\mu,\mathbf{k}} \langle \mu\mathbf{k} | \hat{\mathcal{J}} | \mu\mathbf{k} \rangle n_{\mu,\mathbf{k}}(t), \quad (11)$$

from the numerical solution of Eq. (8). The hole spin relaxation time can be extracted from the exponential fitting of \mathcal{J} with respect to time. One further calculates the concerned coefficients such as α , β , A_{ss} and A_{ss}^v .

III. NUMERICAL RESULTS

In the Zener model, the sp - d exchange interaction constants J_{ex}^{mm} are important parameters for the band structure. In the experimental works, the p - d exchange coupling constant J_{ex}^{pp} was reported to vary from -1 eV to 2.5 eV, depending on the doping density.^{39–41} In ferromagnetic samples, J_{ex}^{pp} is believed to be negative, which was demonstrated by theoretical estimation $J_{\text{ex}}^{pp} \approx -0.3$ eV (Ref. 42). In our calculation, the antiferromagnetic p - d interaction J_{ex}^{pp} is chosen to be -0.5 eV or -1.0 eV. The ferromagnetic s - d exchange coupling constant is taken to be $J_{\text{ex}}^{ss} = 0.2$ eV (Ref. 31).

Another important quantity for determining the Zeeman splitting is the macroscopic magnetization or the effective concentration of the Mn atoms. As deduced from the low-temperature saturate magnetization, only around 50 % Mn atoms can contribute to the ferromagnetic magnetization, which has been recognized as the influence of the compensation effect due to the deep donors (e.g., As antisites) or the formation of sixfold-coordinated centers defect $\text{Mn}^{6\text{As}}$ (Ref. 43). As only the uncompensated Mn atoms can supply holes and contribute to the ferromagnetic magnetization,⁴⁴ one can also estimate the total hole density from the saturate magnetization.⁴⁵ However, the density of the itinerant hole can be smaller than the effective Mn concentration because of the localized effect in such disordered material. It was reported

	T_c (K)	M_s (emu·cm ⁻³)	N_{Mn} (10 ²⁰ cm ⁻³)
A ^a	130	38	8
B ^a	157	47	10
C ^b	114	33	6.9
D ^c	110	—	—
E ^d	139	53.5	11.5

^a Ref. 21, ^b Ref. 23, ^c Ref. 18, ^d Ref. 45

TABLE I: The parameters obtained from the experiments for different samples: A: Ga_{0.93}Mn_{0.07}As/Ga_{0.902}In_{0.098}As; B: Ga_{0.93}Mn_{0.07}As/GaAs; C: Ga_{0.93}Mn_{0.07}As/Ga_{1-y}In_yAs; D: Ga_{0.92}Mn_{0.08}As; E: Ga_{0.896}Mn_{0.104}As_{0.93}P_{0.07}. M_s stands for the saturate magnetization at zero temperature $M(0)$.

that the hole density is only 15-30 % of the total concentration of the Mn atoms.⁴³

In our calculation, the magnetization lies along the principle axis chosen as [001]-direction.³¹ The conventional parameters are mainly taken from those of GaAs in Refs.46 and 47. Other sample-dependent parameters such as the Curie temperature and effective Mn concentration are picked up from the experimental works.^{18,21,23,45} For sample A, B and E (C), only the saturate magnetization at 4 (104) K was given in the references. Nevertheless, one can extrapolate the zero temperature magnetization M_s from Eq. (5). The effective Mn concentrations listed in Table I are derived from $N_{\text{Mn}} = M_s / (g\mu_B S_d)$. It is clear to see that all of these effective Mn concentrations are much smaller than the doping density ($\geq 1.5 \times 10^{21}$ cm⁻³) due to the compensation effect as discussed above. Since the saturate magnetization of sample D is unavailable, we treat the effective Mn concentration as a parameter in this case. Moreover, since the exact values of the itinerant hole densities are unclear in such strongly disordered samples, we treat them as parameters. Two typical values are chosen in our numerical calculation, i.e., $N_h = 3 \times 10^{20}$ cm⁻³ and 5×10^{20} cm⁻³. The effective impurity density is taken to be equal to the itinerant hole density.

For numerical calculation of the hole spin dynamics, the momentum space is partitioned into blocks. Compared to the isotropic parabolic dispersion, the band structure in ferromagnetic GaMnAs is much more complex as we mentioned above [referred to Figs.1(b) and 4]. Therefore, we need to extend the partition scheme used in isotropic parabolic dispersion⁴⁸ into anisotropic case. In our scheme, the radial partition is still carried out with respect to the equal-energy shells, while the angular partition is done by following Ref.48. In contrast to the isotropic case, the number of states in one block is generally different from that in another block even both of them are on the same equal-energy shell. We calculate the number of states of each block from its volume in

momentum space.

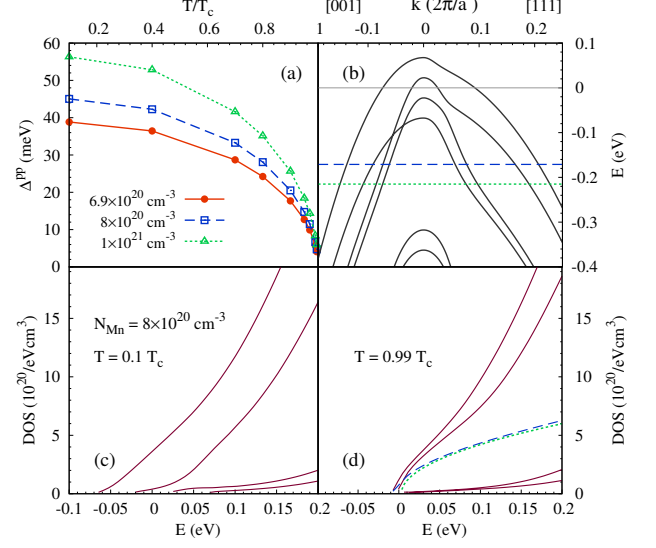


FIG. 1: (Color online) (a) Zeeman energy as function of temperature. (b) The valence band structure with $\Delta^{pp} = 45$ meV. The blue dashed curve illustrates the Fermi level for the hole density $N_h = 3 \times 10^{20}$ cm⁻³, while the green dotted one gives $N_h = 5 \times 10^{20}$ cm⁻³. The density of states as function of energy at (c) $T/T_c = 0.1$ and (d) $T/T_c = 0.99$ for the uncompensated Mn density $N_{\text{Mn}} = 8 \times 10^{21}$ cm⁻³. In (d), the blue dashed curve stands for the upper heavy hole band from the spherical approximation and the corresponding DOS from the analytical formula $(\sqrt{2E}[\sqrt{m^*}/(2\pi\hbar)]^3)$ is given as the green dotted curve. Here, $J_{\text{ex}}^{pp} = -0.5$ eV.

A. Density of states

By solving Eq.(5), one obtains the magnetization at finite temperature $M(T)$ and the corresponding Zeeman energy Δ^{pp} . In Fig.1(a), the Zeeman splitting from $J_{\text{ex}}^{pp} = -0.5$ eV is plotted as function of the temperature. It is seen that the Zeeman energy is tens of milli-electron volts at low temperature and decreases sharply near the Curie temperature due to the decrease of the magnetization. To show the anisotropic nonparabolic feature of the band structure in the presence of the Zeeman splitting, we illustrate the valence bands along [001]- and [111]-directions in Fig.1(b), which are obtained from Eq.(6) at $T/T_c = 0.1$ for $N_{\text{Mn}} = 8 \times 10^{20}$ cm⁻³. In this case, the Zeeman splitting $\Delta^{pp} = 45$ meV. The Fermi levels for the hole densities $N_h = 3 \times 10^{20}$ cm⁻³ and 5×10^{20} cm⁻³ are shown as blue dashed and green dotted curves, respectively. As one can see that all of the four upper bands can be occupied and the effective mass approximation obviously breaks down.

By integrating over the volume of each equal-energy shell, one obtains the density of states (DOS) of each band as function of energy in Fig. 1(c) and (d). Here the energy is defined in the hole picture so that the sign of

the energy is opposite to that in Fig. 1(b). It is seen that the DOS of the upper two bands are much larger than those of the other bands, regardless of the magnitude of the Zeeman splitting. For $T/T_c = 0.99$, the systems approach the paramagnetic phase and the nonparabolic effect is still clearly seen from the DOS in Fig. 1(d), especially in the high energy regime. Moreover, the pronounced discrepancy of the DOS for the two heavy hole bands suggests the finite splitting between them. We find that these features are closely connected with the anisotropy of the valence bands, corresponding to the Luttinger parameters $\gamma_2 \neq \gamma_3$ in GaAs.⁴⁹ In our calculation, we take $\gamma_1 = 6.85$, $\gamma_2 = 2.1$ and $\gamma_3 = 2.9$ from Ref. 47. As a comparison, we apply a spherical approximation ($\gamma_1 = 6.85$ and $\gamma_2 = \gamma_3 = \bar{\gamma} = 2.5$) and find that the two heavy hole bands become approximately degenerate.³⁸ The DOS of the upper heavy hole band is shown as the blue dashed curve in Fig. 1(d), where we also plot the corresponding DOS from the analytical expression, i.e., $\sqrt{2E}[\sqrt{m^*}/(2\pi\hbar)]^3$, as the green dotted curve. Here, we use the heavy-hole effective mass $m^* = m_0/(\gamma_1 - 2\bar{\gamma})$ with m_0 denoting the free electron mass. The perfect agreement between the analytical and our numerical results under the spherical approximation suggests the good precision of our numerical scheme.

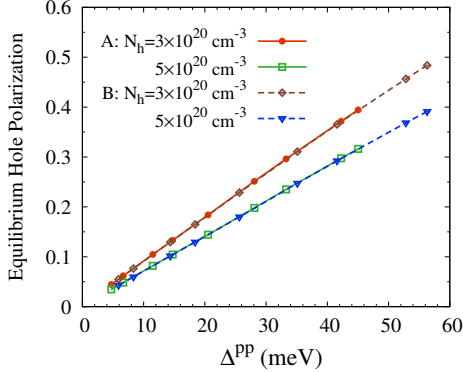


FIG. 2: (Color online) The equilibrium hole spin polarization as function of Zeeman splitting for sample A and B. Here, $J_{\text{ex}}^{\text{pp}} = -0.5$ eV.

B. Hole spin relaxation

In this part, we investigate the hole spin dynamics by numerically solving the microscopic kinetic equation, i.e., Eq. (8). By taking into account the equilibrium hole spin polarization, we fit the temporal evolution of the total spin polarization along [001]-direction by

$$\mathcal{J}_z(t) = \mathcal{J}_z^0 + \mathcal{J}_z' e^{-t/\tau_s}, \quad (12)$$

where \mathcal{J}_z^0 and \mathcal{J}_z' correspond to the equilibrium and non-equilibrium spin polarizations, respectively. τ_s is the hole spin relaxation time.

In all the cases of the present work, the equilibrium hole spin polarization for a fixed hole density is found to be approximately linearly dependent on the Zeeman splitting. In Fig. 2, \mathcal{J}_z^0 in samples A and B (similar behavior for others) are plotted as function of Zeeman splitting, where the exchange coupling constant $J_{\text{ex}}^{\text{pp}}$ is taken to be -0.5 eV. One notices that the average spin polarization becomes smaller with the increase of the hole density, reflecting the large interband mixing for the states in the high energy regime.

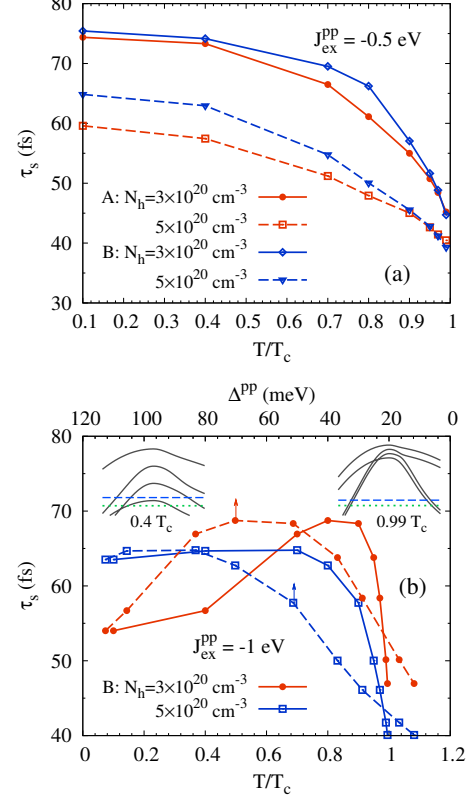


FIG. 3: (Color online) (a) Spin relaxation time as function of temperature with $J_{\text{ex}}^{\text{pp}} = -0.5$ eV for sample A and B. (b) Spin relaxation time as function of temperature and Zeeman splitting obtained from the calculation with $J_{\text{ex}}^{\text{pp}} = -1$ eV for sample B. The inset at the left (right) upper corner illustrates the band structure from [001]-direction to [111]-direction [refer to Fig. 1(b)] for $T/T_c = 0.4$ (0.99) and $\Delta^{\text{pp}} = 105$ (16.7) meV. The Fermi levels of $N_h = 3 \times 10^{20} \text{ cm}^{-3}$ and $5 \times 10^{20} \text{ cm}^{-3}$ are shown as the blue dashed and green dotted curves in the insets, separately.

The temperature dependence of the hole spin relaxation time in samples A and B with $J_{\text{ex}}^{\text{pp}} = -0.5$ eV is shown in Fig. 3(a), where the spin relaxation time monotonically decreases with increasing temperature. This feature can be understood from the enhancement of the interband mixing as the Zeeman splitting decreases (shown below).⁵⁰ To gain a complete picture of the role of the Zeeman splitting on the hole spin relaxation in fer-

romagnetic GaMnAs, we also carry out the calculation with the exchange constant $J_{\text{ex}}^{pp} = -1$ eV.^{31,39} Very interestingly, one finds that the hole spin relaxation time at low temperature increases with increasing temperature, resulting in a nonmonotonic temperature dependence of the hole spin relaxation time in sample B. The results in this case are shown as solid curves in Fig. 3(b), where we also plot the Zeeman splitting dependence of the hole spin relaxation time as dashed curves. It is seen that the hole spin relaxation time for the hole density $N_h = 3 \times 10^{20} \text{ cm}^{-3}$ first increases with increasing temperature (alternatively speaking, decreasing Zeeman splitting) and starts to decrease at around $0.8 T_c$ where the Zeeman splitting $\Delta^{pp} = 70$ meV. To understand this feature, we show the typical band structure in the increase (decrease) regime of the hole relaxation time at $T/T_c = 0.4$ (0.99), corresponding to $\Delta^{pp} = 105$ (16.7) meV, in the inset at the left (right) upper corner. The Fermi levels of the hole density $3 \times 10^{20} \text{ cm}^{-3}$ are labeled by blue dashed curves. One finds that the carrier occupations in the increase and decrease regimes are quite different. Specifically, all of the four upper bands are occupied in the decrease regime while only three valence bands are relevant in the increase regime.

One may naturally expect that the increase regime originates from the contribution of the fourth band via the inclusion of the additional scattering channels or the modification of the screening. However, we rule out this possibility through the computation with the fourth band artificially excluded, where the results are qualitatively the same as those in Fig. 3(b). Moreover, the variations of the screening and the equilibrium distribution at finite temperature are also demonstrated to be irrelevant to the present nonmonotonic dependence by our calculation (not shown here). Therefore, the interesting feature has to be attributed to the variations of the band distortion and spin mixing due to the exchange interaction. This is supported by our numerical calculation, where the nonmonotonic behavior disappears once the effect of the interband mixing is excluded by removing the wavefunction overlaps $|\langle \mu \mathbf{k} | \nu \mathbf{k}' \rangle|^2$ in Eqs. (9) and (10) (not shown here).

For a qualitative understanding of the nonmonotonic temperature dependence of the hole spin relaxation time, we plot the Fermi surface in the k_x - k_z ($k_y = 0$) and k_x - k_y ($k_z = 0$) planes at $N_h = 3 \times 10^{20} \text{ cm}^{-3}$ in Fig. 4. We choose typical Zeeman splittings in the increase regime ($\Delta^{pp} = 105$ meV), the decrease regime ($\Delta^{pp} = 16.7$ meV) and also the crossover regime ($\Delta^{pp} = 70$ meV). One notices that the Fermi surfaces in Fig. 4(a) and (d) are composed of three closed curves, meaning that only three bands are occupied for $\Delta^{pp} = 105$ meV [also see the inset of Fig. 3(b)]. For the others with smaller Zeeman splittings, all of the four upper bands are occupied. The spin expectation of each state at Fermi surface is represented by the color coding. Note that the spin expectation of the innermost band for $\Delta^{pp} = 70$ meV is close to -1.5 [see Fig. 4(b) and (e)], suggesting that this band is

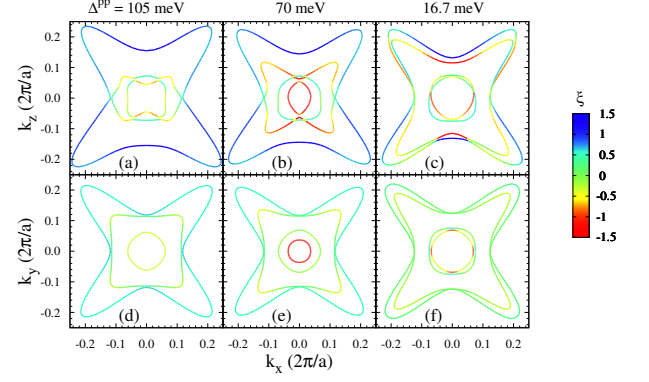


FIG. 4: (Color online) The Fermi surface in the k_x - k_z ($k_y = 0$) and k_x - k_y ($k_z = 0$) planes with $\Delta^{pp} = 105$ meV (a,d), 70 meV (b,e) and 16.7 meV (c,f). The color coding represents the spin expectation of each state, $\xi = \langle \mu | \mathcal{J}_z | \mu \rangle$. Here, $N_h = 3 \times 10^{20} \text{ cm}^{-3}$.

the spin-down heavy hole band and the mixing of other spin components in this band is marginal. Therefore, the spin-flip scattering related to this band is weak and can not result in the increase of the hole spin relaxation time mentioned above. By comparing the results with $\Delta^{pp} = 105$ meV and 70 meV, one notices that the spin expectation of the Fermi surface of the outermost band is insensitive to the Zeeman splitting. Therefore, this band can not be the reason of the increase regime also. Moreover, for the second and third bands in Fig. 4(a) and (b), from the comparable color coding between the two figures in this regime [also see Fig. 4(d) and (e) with $k_z = 0$], one finds that the spin expectation for the states with small k_z is also insensitive to the Zeeman splitting. However, for the states with large k_z , the spin expectation of the spin-down states ($\xi < 0$) approaches a large magnitude (-1.5) with decreasing Zeeman splitting, suggesting the decrease of the mixing from the spin-up states. As a result, the interband spin-flip scattering from/to these states becomes weak and the hole spin relaxation time increases. In the decrease regime of the hole spin relaxation time, Fig. 4(c) and (f) show that the two outer/inner bands approach each other, leading to a strong and anisotropic spin mixing. Therefore, the spin-flip scattering becomes more efficient in this regime and the spin relaxation time decreases. One may suppose that the nonmonotonic temperature dependence of the hole spin relaxation time can also arise from the variation of the shape of the Fermi surface, according to Fig. 4. However, this variation itself is not the key of the nonmonotonic behavior, because the calculation with this effect but without band mixing can not recover the nonmonotonic feature as mentioned in the previous paragraph. For the hole density $N_h = 5 \times 10^{20} \text{ cm}^{-3}$, the structures of the Fermi surface at $\Delta^{pp} = 105$ meV are similar to those in Fig. 4(b) and (e). This explains the absence of the increase regime for this density in Fig. 3(b).

Moreover, we should point out that the increase regime

of the hole spin relaxation time in sample A for $J_{\text{ex}}^{pp} = -1$ eV is much narrower than that in sample B. The reason lies in the fact of lower effective Mn density in sample A, leading to the smaller maximal Zeeman splitting ~ 90 meV, only slightly larger than the crossover value 70 meV at $N_h = 3 \times 10^{20} \text{ cm}^{-3}$.

As a summary of this part, we find different temperature dependences of the hole spin relaxation time due to the different values of effective Mn concentration, hole density and exchange coupling constant J_{ex}^{pp} . In the case with large coupling constant and high effective Mn concentration, the interband spin mixing can result in a non-monotonic temperature dependence of the hole spin relaxation time. Our results suggest a possible way to estimate the exchange coupling constant with the knowledge of itinerant hole density, i.e., by measuring the temperature dependence of the hole spin relaxation time. Alternatively, the discrepancy between the hole relaxation time from different hole densities in Fig. 3(b) suggests that one can also estimate the itinerant hole density if the exchange coupling constant has been measured from other methods.

C. Gilbert damping and non-adiabatic torque coefficients

Facilitated with the knowledge of the hole spin relaxation time, we can calculate the coefficients in the LLG equation. According to our previous works,^{10,17} the Gilbert damping and nonadiabatic spin torque coefficients can be expressed as

$$\alpha = J_h / [N_{\text{Mn}} |\langle \mathbf{S} \rangle| (\beta + 1/\beta)], \quad (13)$$

and

$$\beta = 1 / (2\tau_s \Delta^{pp}), \quad (14)$$

respectively. In Eq. (13), J_h represents the total equilibrium spin polarization of the itinerant hole gas, i.e., $J_h = N_h \mathcal{J}_z^0$ with \mathcal{J}_z^0 being the one defined in Eq. (12) in our study. The average spin polarization of a single Mn ion is given by $|\langle \mathbf{S} \rangle| = S_d M(T) / M(0)$.

In Fig. 5(a), (c) and (e), the nonadiabatic spin torque coefficients β in sample A-C are plotted as function of temperature with $J_{\text{ex}}^{pp} = -0.5$ eV and -1.0 eV. Our results in sample C show good agreement with the experimental data (plotted as the brown square) in Fig. 5(e).²³ At low temperature, the value of β is around 0.1~0.3, which is also comparable with the previous theoretical calculation.¹⁹ Very interestingly, one finds that β sharply increases when the temperature approaches the Curie temperature. This can be easily understood from the pronounced decreases of the spin relaxation time and the Zeeman splitting in this regime [see Figs. 1(a) and 3]. By comparing the results with different values of the exchange coupling constant, one finds that β from $J_{\text{ex}}^{pp} = -1$ eV is generally about one half of that obtained from $J_{\text{ex}}^{pp} = -0.5$ eV because of the larger Zeeman

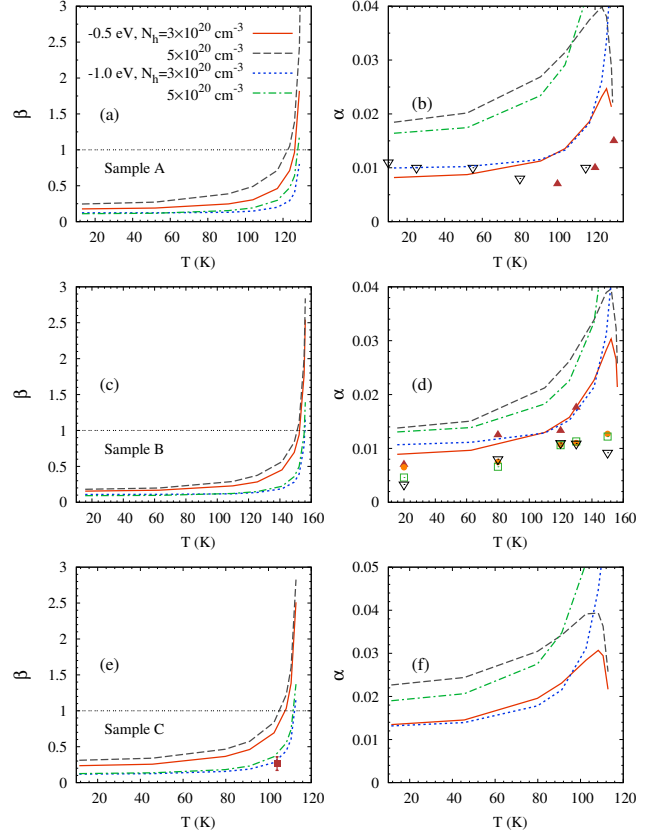


FIG. 5: (Color online) β and α as function of temperature with $J_{\text{ex}}^{pp} = -0.5$ eV and -1.0 eV in sample A-C. In (b) and (d), the dots represent the experimental data from ferromagnetic resonance measurement for [001] (brown solid upper triangles), [110] (orange solid circles), [100] (green open squares) and [1-10] (black open lower triangles) dc magnetic-field orientations (Ref. 21). The brown solid square in (e) stands for the experimental result from domain-wall motion measurement (Ref. 23).

splitting. Moreover, one notices that the nonmonotonic temperature dependence of the hole spin relaxation time in Fig. 3(b) is not reflected in β due to the influence of the Zeeman splitting. In all cases, the values of β can exceed one very near the Curie temperature.

The results of the Gilbert damping coefficient from Eq. (13) are shown as curves in Fig. 5(b), (d) and (f). The dots in these figures are the reported experimental data from the ferromagnetic resonance along different magnetic-field orientations.²¹ Both the magnitude and the temperature dependence of our results agree well with the experimental data. From Fig. 2, one can conclude that the prefactor in Eq. (13), $J_h / (N_{\text{Mn}} |\langle \mathbf{S} \rangle|)$, is almost independent of temperature. Therefore, the temperature dependence of α mainly results from the nonadiabatic spin torque coefficient β . Specifically, α is insensitive to the temperature in the low temperature regime and it gradually increases with increasing temperature due

to the increase of β . Moreover, we predict that α begins to decrease with increasing temperature once β exceeds one. This crossover lying at $\beta \approx 1$ can be expected from Eq. (13). By comparing the results with different values of J_{ex}^{pp} , one finds that the value of α is robust against the exchange coupling constant in the low temperature regime. In this regime, $\beta \ll 1$ and one can simplify the expression of the Gilbert damping coefficient as $\alpha \approx \frac{N_h}{N_{\text{Mn}} S_d} \frac{\mathcal{J}_z^0}{(\tau_s \Delta^{pp})}$. Since the total hole spin polarization is proportional to the Zeeman splitting (see Fig. 2) and τ_s is only weakly dependent on the Zeeman splitting (see Fig. 3) in this regime, the increase of J_{ex}^{pp} does not show significant effect on α . However, at high temperature, the scenario is quite different. For example, one has the maximum of the Gilbert damping coefficient $\alpha_m \approx \frac{N_h}{2N_{\text{Mn}} |\langle \mathbf{S} \rangle|} \mathcal{J}_z^0 \propto J_{\text{ex}}^{pp}$ at $\beta = 1$.

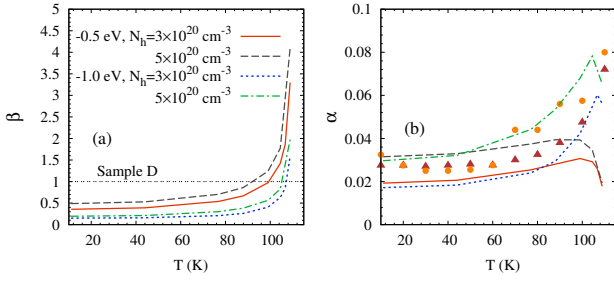


FIG. 6: (Color online) β and α as function of temperature by taking $N_{\text{Mn}} = 5 \times 10^{20} \text{ cm}^{-3}$ with $J_{\text{ex}}^{pp} = -0.5 \text{ eV}$ and -1.0 eV in sample D. The dots are from ferromagnetic resonance measurement (Ref. 18) for [001] (brown solid upper triangles) and [110] (orange solid circles) dc magnetic-field orientations.

Since the effective Mn concentration of sample D is unavailable as mentioned above, we here take $N_{\text{Mn}} = 5 \times 10^{20} \text{ cm}^{-3}$. The results are plotted in Fig. 6. It is seen that the Gilbert damping coefficients from our calculation with $J_{\text{ex}}^{pp} = -1 \text{ eV}$ agree with the experiment very well. As reported, the damping coefficient in this sample is much larger (~ 0.1) before annealing.¹⁸ The large Gilbert damping coefficient in the as-grown sample may result from the direct spin-flip scattering between the holes and the random Mn spins, existing in low quality samples. In the presence of this additional spin-flip channel, the hole spin relaxation time becomes shorter and results in an enhancement of α and β (for $\beta < 1$). Moreover, in the low temperature regime, a decrease of the Gilbert damping coefficient was observed by increasing temperature,¹⁸ which is absent in our results. This may originate from the complicated localization or correlation effects in such a disordered situation. The quantitatively microscopic study in this case is beyond the scope of the present work.

In addition, one notices that β in Ref. 24 was determined to be around 0.01, which is one order of magnitude smaller than our result. The reason is because of the incorrect parameter used in that work, as pointed out

by Adam *et al.*²³

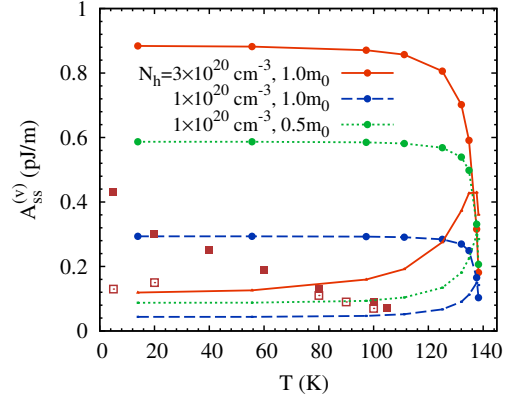


FIG. 7: (Color online) Spin stiffness (vertical spin stiffness) coefficient as function of temperature is plotted as curves with (without) symbols. The calculation is carried out with $J_{\text{ex}}^{pp} = -0.5 \text{ eV}$ in sample E. The effective mass is taken to be 1.0 (0.5) m_0 as labeled in the figure. The brown solid (from the period of the domains) and open (from the hysteresis cycle) squares are the experimental data of spin stiffness from Ref. 45.

D. Spin stiffness and vertical spin stiffness

In this subsection, we calculate the spin stiffness and vertical spin stiffness coefficients according to our previous derivation¹⁰

$$A_{\text{ss}} = N_h / [4m^*(1 + \beta^2)] \quad (15)$$

and

$$A_{\text{ss}}^{(v)} = N_h \beta / [4m^*(1 + \beta^2)]. \quad (16)$$

Since the effective mass m^* is a rough description for the anisotropic valence bands in the presence of a large Zeeman splitting, it is difficult to obtain the accurate value of the stiffness coefficients from these formulas. Nevertheless, one can still estimate these coefficients with the effective mass taken as a parameter. The results are plotted in Fig. 7. By fitting the DOS of the occupied hole states, we find $m^* \approx m_0$, which is consistent with the previous work.³¹ The spin stiffness and vertical spin stiffness coefficients with $N_h = 3 \times 10^{20} \text{ cm}^{-3}$ ($1 \times 10^{20} \text{ cm}^{-3}$) are plotted as the red solid (blue dashed) curves with and without symbols, respectively. The sudden decrease of A_{ss} originates from the increase of β in the vicinity of the Curie temperature (see Fig. 5). Our results are comparable with the previous theoretical work from 6-band model.²⁶ As a comparison, we take $m^* = 0.5m_0$, which is widely used to describe the heavy hole in the low energy regime in the absence of the Zeeman splitting.⁵¹ The spin stiffness becomes two times larger. Moreover,

A_{ss}^v is found to present a nonmonotonic behavior in the temperature dependence as predicted by Eq. (16).

In Fig. 7, we also plot the experimental data of the spin stiffness coefficient from Ref. 45. It is seen that these values of A_{ss} are comparable with our results and show a decrease as the temperature increases. However, one notices that the experimental data is more sensitive to the temperature especially for those determined from the domain period in the low temperature regime. This may originate from the strong anisotropic interband mixing and inhomogeneity in the real material.

In Ref. 10, we have shown that the vertical spin stiffness can lead to the magnetization rotated around the easy axis within the domain wall structure by $\Delta\varphi = (\sqrt{1 + \beta^2} - 1)/\beta$ in the absence of the demagnetization field. For $\beta = 1$, $\Delta\varphi \approx 0.13\pi$, while $\Delta\varphi = \beta/2 \rightarrow 0$ for $\beta \ll 1$. As illustrated above, β is always larger than 0.1. Therefore, the vertical spin stiffness can present observable modification of the domain wall structure in GaMnAs system.¹⁰

IV. SUMMARY

In summary, we theoretically investigate the temperature dependence of the LLG coefficients in ferromagnetic GaMnAs, based on the microscopic calculation of the hole spin relaxation time. In our calculation, we employ the Zener model with the band structure carried out by diagonalizing the 8×8 Kane Hamiltonian together with the Zeeman energy due to the *sp-d* exchange interaction. We find that the hole spin relaxation time can present different temperature dependences, depending on the ef-

fective Mn concentration, hole density and exchange coupling constant. In the case with high Mn concentration and large exchange coupling constant, the hole spin relaxation time can be nonmonotonically dependent on temperature, resulting from the different interband spin mixings in the large and small Zeeman splitting regimes. These features are proposed to be for the estimation of the exchange coupling constant or itinerant hole density. By substituting the hole relaxation time, we calculate the temperature dependence of the Gilbert damping, nonadiabatic spin torque, spin stiffness, and vertical spin stiffness coefficients. We obtain the nonadiabatic spin torque coefficient around $0.1 \sim 0.3$ at low temperature, which is consistent with the experiment. As the temperature increases, this coefficient shows a monotonic increase. In the low temperature regime, the Gilbert damping coefficient increases with temperature, which shows good agreement with the experiments. We predict that the Gilbert damping coefficient can decrease with increasing temperature once the nonadiabatic spin torque coefficient exceed one in the vicinity of the Curie temperature. We also find that the spin stiffness decreases with increasing temperature and the vertical spin stiffness can present a nonmonotonic temperature dependence, similar to the Gilbert damping.

Acknowledgments

This work was supported by the National Natural Science Foundation of China under Grant No. 10725417 and the National Basic Research Program of China under Grant No. 2012CB922002.

* Author to whom correspondence should be addressed; Electronic address: mwwu@ustc.edu.cn.

¹ H. Ohno, Science **281**, 951 (1998).

² T. Jungwirth, J. Sinova, J. Mašek, J. Kučera, and A. H. MacDonald, Rev. Mod. Phys. **78**, 809 (2006).

³ M. G. Pala, M. Governale, J. König, U. Zülicke, and G. Iannaccone, Phys. Rev. B **69**, 045304 (2004).

⁴ M. Ciorga, A. Einwanger, U. Wurstbauer, D. Schuh, W. Wegscheider, and D. Weiss, Phys. Rev. B **79**, 165321 (2009).

⁵ T. L. Gilbert, Phys. Rev. **100**, 1243 (1955).

⁶ L. D. Landau, E. M. Lifshitz, and L. P. Pitaevski, *Statistical Physics*, Part 2, 3rd ed. (Pergamon, Oxford, 1980).

⁷ L. Berger, Phys. Rev. B **33**, 1572 (1986).

⁸ S. Zhang and Z. Li, Phys. Rev. Lett. **93**, 127204 (2004).

⁹ G. Tatara, H. Kohno, and J. Shibata, Phys. Rep. **468**, 213 (2008).

¹⁰ K. Shen, G. Tatara, and M. W. Wu, Phys. Rev. B **83**, 085203 (2011).

¹¹ F. Piéchon and A. Thiaville, Phys. Rev. B **75**, 174414 (2007).

¹² H. Kohno, G. Tatara, and J. Shibata, J. Phys. Soc. Jpn. **75**, 113706 (2006).

¹³ H. Kohno and J. Shibata, J. Phys. Soc. Jpn. **76**, 063710 (2007).

¹⁴ J. Kuneš and V. Kambarský, Phys. Rev. B **65**, 212411 (2002).

¹⁵ D. Steiauf and M. Fähnle, Phys. Rev. B **72**, 064450 (2005).

¹⁶ Y. Tserkovnyak, G. A. Fiete, and B. I. Halperin, Appl. Phys. Lett. **84**, 5234 (2004).

¹⁷ K. Shen, G. Tatara, and M. W. Wu, Phys. Rev. B **81**, 193201 (2010).

¹⁸ J. Sinova, T. Jungwirth, X. Liu, Y. Sasaki, J. K. Furdyna, W. A. Atkinson, and A. H. MacDonald, Phys. Rev. B **69**, 085209 (2004).

¹⁹ Ion Garate, K. Gilmore, M. D. Stiles, and A. H. MacDonald, Phys. Rev. B **79**, 104416 (2009).

²⁰ K. M. D. Hals, A. K. Nguyen, and A. Brataas, Phys. Rev. Lett. **102**, 256601 (2009).

²¹ Kh. Khazen, H. J. von Bardeleben, M. Cubukcu, J. L. Cantin, V. Novak, K. Olejnik, M. Cukr, L. Thevenard, and A. Lemaître, Phys. Rev. B **78**, 195210 (2008).

²² J. Qi, Y. Xu, N. H. Tolk, X. Liu, J. K. Furdyna, I. E. Perakis, Appl. Phys. Lett. **91**, 112506 (2007).

²³ J.-P. Adam, N. Vernier, J. Ferré, A. Thiaville, V. Jeudy, A. Lemaître, L. Thevenard, and G. Faini, Phys. Rev. B

- 80**, 193204 (2009).
- ²⁴ M. Yamanouchi, D. Chiba, F. Matsukura, T. Dietl, and H. Ohno, Phys. Rev. Lett. **96**, 096601 (2006).
 - ²⁵ J. König, H. H. Lin, and A. H. MacDonald, Physica E **10**, 139 (2001).
 - ²⁶ J. König, T. Jungwirth, and A. H. MacDonald, Phys. Rev. B **64**, 184423 (2001).
 - ²⁷ C. Zener, Phys. Rev. **81**, 440 (1951).
 - ²⁸ T. Dietl, H. Ohno, F. Matsukura, J. Cibert, and D. Fer-
rand, Science **287**, 1019 (2000).
 - ²⁹ M. Abolfath, T. Jungwirth, J. Brum, A. H. MacDonald,
Phys. Rev. B **63**, 054418 (2001)
 - ³⁰ T. Dietl, Nature Mater. **9**, 965 (2010).
 - ³¹ L. Cywiński and L. J. Sham, Phys. Rev. B **76**, 045205
(2007).
 - ³² E. O. Kane, J. Phys. Chem. Solids **1**, 249 (1957).
 - ³³ M. I. Darby, J. Appl. Phys. **18**, 1415 (1967).
 - ³⁴ J. Schliemann, Phys. Rev. B **74**, 045214 (2006).
 - ³⁵ M. W. Wu, J. H. Jiang, and M. Q. Weng, Phys. Rep. **493**,
61 (2010).
 - ³⁶ M. Q. Weng and M. W. Wu, Phys. Rev. B **68**, 075312
(2003).
 - ³⁷ J. Zhou, J. L. Cheng, and M. W. Wu, Phys. Rev. B **75**,
045305 (2007).
 - ³⁸ K. Shen and M. W. Wu, Phys. Rev. B **82**, 115205 (2010).
 - ³⁹ K. S. Burch, D. D. Awschalom, and D. N. Basov, J. Magn.
Magn. Mater. **320**, 3207 (2008).
 - ⁴⁰ J. Okabayashi, A. Kimura, O. Rader, T. Mizokawa, A.
Fujimori, T. Hayashi, and M. Tanaka, Phys. Rev. B **58**,
R4211 (1998).
 - ⁴¹ W. Heimbrodt, Th. Hartmann, P. J. Klar, M. Lampalzer,
W. Stolz, K. Volz, A. Schaper, W. Treutmann, H. -A. Krug
von Nidda, A. Loidl, T. Ruf, and V. F. Sapega, Physica E
10, 175 (2001).
 - ⁴² J. M. Tang and M. E. Flatté, Phys. Rev. Lett. **92**, 047201
(2004).
 - ⁴³ R. R. dos Santos, L. E. Oliveira, and J. Castro, J. Phys.:
Condens. Matter **14**, 3751 (2002).
 - ⁴⁴ A. Van Esch, L. Van Bockstal, J. De Boeck, G. Verbanck,
A. S. van Steenbergen, P. J. Wellmann, B. Grietens, R.
Bogaerts, F. Herlach, and G. Borghs, Phys. Rev. B **56**,
13103 (1997).
 - ⁴⁵ S. Haghgoo, M. Cubukcu, H. J. von Bardeleben, L. Theve-
nard, A. Lemaître, and C. Gourdon, Phys. Rev. B **82**,
041301 (2010).
 - ⁴⁶ *Semiconductors*, edited by O. Madelung (Springer-Verlag,
Berlin, 1987), Vol. 17a.
 - ⁴⁷ R. Winkler, *Spin-Orbit Coupling Effects in Two-
Dimensional Electron and Hole Systems* (Springer, Berlin,
2003).
 - ⁴⁸ J. H. Jiang and M. W. Wu, Phys. Rev. B **79**, 125206
(2009).
 - ⁴⁹ J. M. Luttinger, Phys. Rev. **102**, 1030 (1956).
 - ⁵⁰ The hole-phonon scattering is rather weak compared
with the hole-impurity scattering in this low tempera-
ture regime. Therefore the pronounced temperature depen-
dence of the hole spin relaxation time can not be explained
by this scattering mechanism.
 - ⁵¹ K. Leo, W. W. Rühle, and K. Ploog, Phys. Rev. B **38**,
1947 (1988).